Available online at www.sciencedirect.com

ScienceDirect

Procedia Structural Integrity 8 (2018) 318–331

Structural Integrity Procedia

www.elsevier.com/locate/procedia

AIAS 2017 International Conference on Stress Analysis, AIAS 2017, 6-9 September 2017, Pisa, Italy

LCF assessment on heat shield components of nuclear fusion experiment "Wendelstein 7-X" by critical plane criteria

V. Giannella[a], R. Citarella[a]*, J. Fellinger[b] and R. Esposito[a]

[a]*Dept. of Industrial Engineering, University of Salerno, via G. Paolo II, 132, Fisciano (SA), Italy*
[b]*Max Planck Institute for Plasma Physics, EURATOM Association, Wendelsteinstr. 1, 17491, Greifswald, Germany*

Abstract

The Wendelstein 7-X modular advanced stellarator has started operations at the Max Planck Institute for Plasma Physics in Greifswald, Germany, in 2016. In the first phase, the machine operated restricting the plasma pulses to low power and short lengths. Plans to achieve actively cooled components are scheduled to start in 2020 when the machine will operate in steady-state at full power. FEM simulations for steady-state operations revealed high plastic strains at several locations, for most of all the rigidly supported Plasma Facing Components; therefore, there is the risk of a premature fatigue failure before the end of the scheduled operations of the machine. The aim of this study is to analyse, by means of the commercial code ABAQUS, the behavior of such critical components estimating, eventually, their fatigue life by means of the commercial code fe-safe.

Peer-review under responsibility of the Scientific Committee of AIAS 2017 International Conference on Stress Analysis

Keywords: Wendelstein 7-X; FEM; Elastic-plastic behavior, Nonlinear hardening; Multiaxial fatigue; fe-safe.

1. Introduction

At the Max Planck Institute for Plasma Physics, Greifswald, Germany, the world's largest nuclear fusion experiment of stellarator type, Wendelstein 7-X (W7-X, Fig. 1a), is currently in operation. The hot hydrogen plasma (torus shaped with major radius of 5.5 m and minor radius of 0.53 m) is confined in a Plasma Vessel (PV) by an

* Corresponding author. Tel.: +39-089-964111; fax: +39-089-964111.
E-mail address: rcitarella@unisa.it

Peer-review under responsibility of the Scientific Committee of AIAS 2017 International Conference on Stress Analysis
10.1016/j.prostr.2017.12.033

Nomenclature

C_i	Hardening parameter for i_{th} linear component
E	Young's modulus
K	thermal conductivity
N_f	number of fatigue cycles
b	Coffin-Manson fatigue strength exponent
c	Coffin-Manson fatigue ductility exponent
c_p	specific heat
α	thermal expansion coefficient
$\boldsymbol{\alpha}$	deviatoric part of the total backstress
$\boldsymbol{\alpha_i}$	deviatoric part of the i_{th} backstress
γ_i	Hardening parameter for i_{th} non linear component
ε'_f	Coffin-Manson fatigue ductility coefficient
$\dot{\varepsilon}_{pl}$	equivalent plastic strain rate
$\dot{\boldsymbol{\varepsilon}}_{\boldsymbol{pl}}$	plastic strain rate
υ	Poisson's ratio
ρ	mass density
σ'_f	Coffin-Manson fatigue strength coefficient
σ_0	initial yield surface size
σ_{YS}	yield stress

electromagnetic (EM) field reaching a magnitude up to 3 T, generated by 50 non-planar and 20 planar superconducting coils (Fig. 1b). The Magnet System (MS) is very rigid to minimize deformations caused by the huge electromagnetic Lorentz forces; this is necessary in order to limit unwanted variation of the magnetic field. The first measurements (Pedersen et al., 2016) of the magnetic field confirmed both accuracy of magnetic field and rigidity of magnetic cage structure.

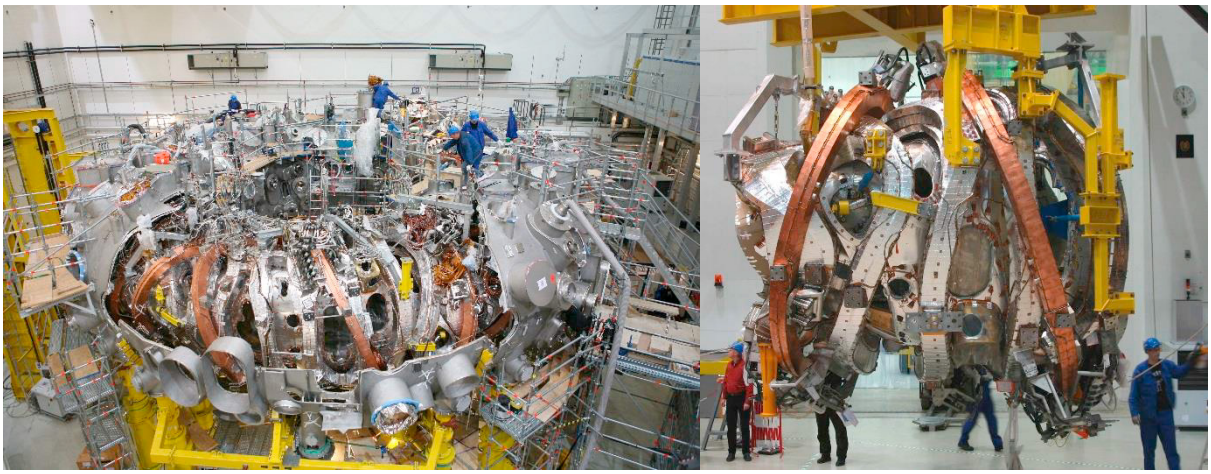

Fig. 1: (a) W7-X Plasma Vessel, (b) W7-X superconducting coils.

In the vacuum created inside the cryostat, the superconducting coils are cooled down to superconducting temperature, close to absolute zero (4 K), using liquid helium. The magnetic cage keeps the 30 cubic meters of ultra-thin plasma suspended inside the PV. Such plasma is heated up to fusion temperature by microwave heating, generated by gyrotrons capable to output up to 1 MW each, allowing for the separation of the electrons from the nuclei of the helium or hydrogen atoms. During the initial operations (Klinger et al., 2017), Operational Phase 1.1

(OP1.1), limiter plasma was produced, with pulse lengths varying from half a second to six seconds and temperatures inside the plasma reaching up to 100 million degrees Celsius.

The subsequent stage to achieve, OP2, adopts actively water-cooled Plasma Facing Components (PFCs) (Fig. 2), in order to protect the PV against the radiative and convective heat fluxes coming from the hot plasma. Depending on the expected heat loads on the different regions of the PV, four types of PFCs will be used:

- highly loaded divertors: made of water-cooled CuCrZr fingers, covered with Carbon Reinforced Composite tiles (Qian et al., 2016);
- moderately loaded heat shields,
- moderately loaded baffles (Fig. 3), both made of CuCrZr heat sinks, brazed on water-cooled steel pipes and covered with bolted graphite tiles. The heat shields are flexibly supported with a few pins onto the PV whereas the baffles are supported by rigid steel structures;
- lowly loaded wall panels, consisting of two parallel steel plates welded together and filled with cooling water.

In the present work the fatigue life of the most critical baffle modules (Fig. 4) is estimated by means of thermomechanical FEM simulations whose outputs are post-processed by the commercial code fe-safe.

In this paper this approach will provide the crack nucleation times, then, further developments are already under implementation for the calculation of the crack propagation times up to the critical crack sizes. The latter calculations refer to the fracture mechanics as implemented through numerical methods as FEM (Citarella et al., 2017), DBEM (Citarella et al., 2015) or coupled FEM-DBEM (Giannella, Fellinger et al., 2017; Giannella, Perrella et al., 2017; Citarella, Lepore et al., 2016, Citarella, Vivo et al., 2016, Citarella et al., 2013), adopted for crack propagation simulations.

Fig. 2: W7-X PV internal view (graphite tiles are not yet assembled).

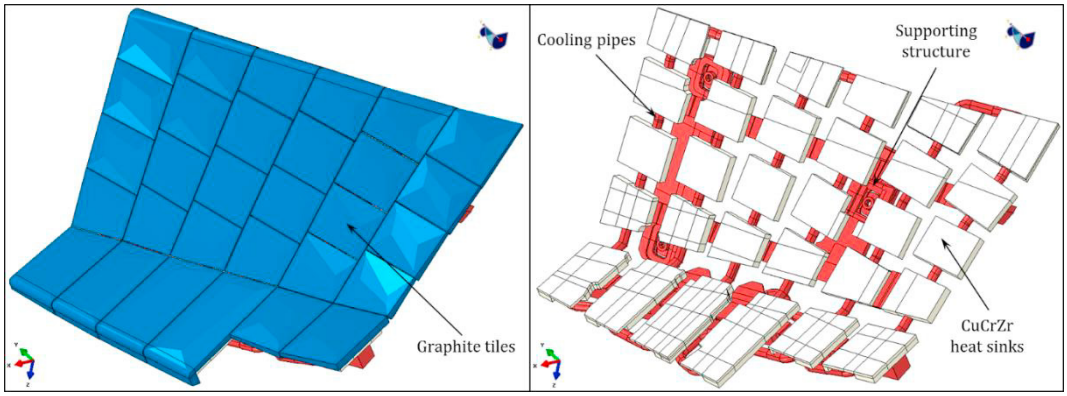

Fig. 3: FEM assembly of Baffle Module BM-7v.

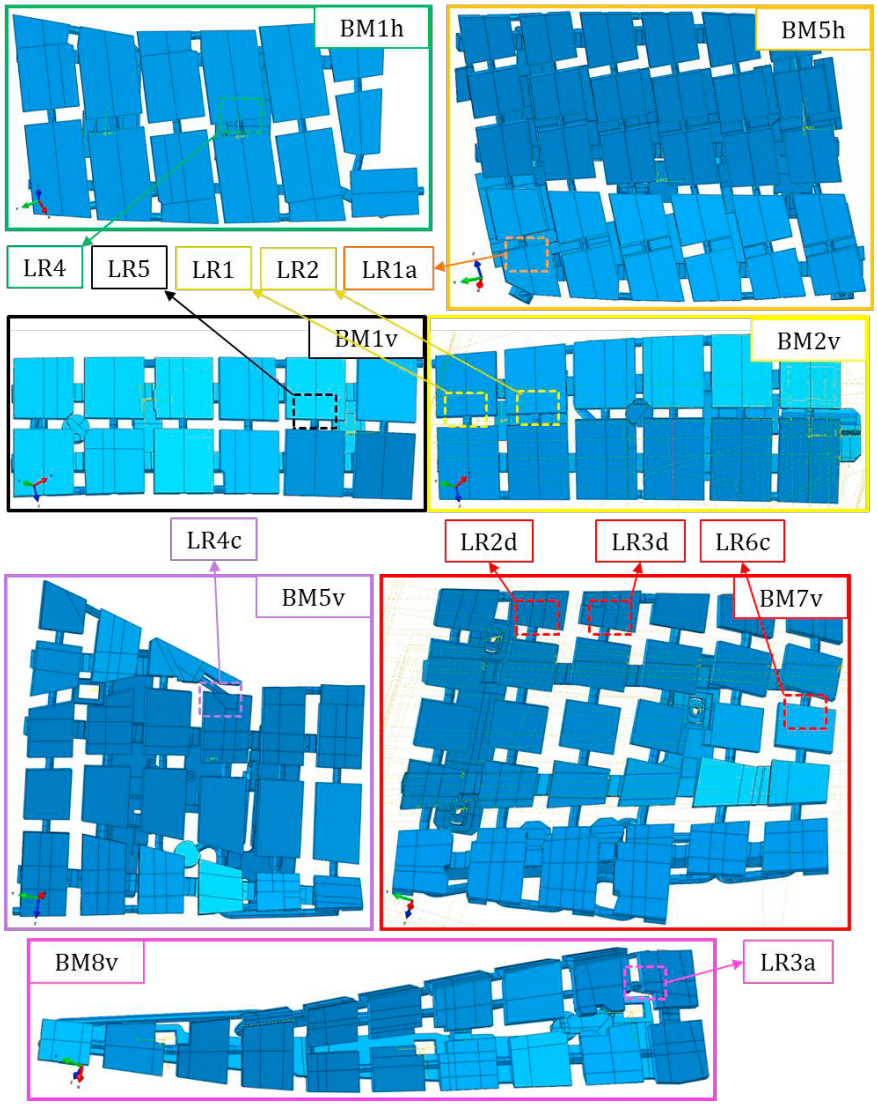

Fig. 4: Analysed baffle modules (BMxx) with the related submodelled locations (LRxx).

Fatigue cracks typically nucleate due to cyclic elastic and plastic strains; therefore, an accurate cyclic plastic hardening assessment is mandatory when dealing with both Low-Cycle (LCF) and High-Cycle Fatigue (HCF).

Several hardening models have been proposed along the years to model the material behavior under LCF conditions. Prager (1956) proposed the simplest kinematic hardening rule, describing the plastic response of materials with a linear correspondence between the yield surface translation and the plastic strain. An improvement was then proposed by Mroz (1967) by adopting a multilinear rule that allowed for a more realistic hysteresis loop simulation. Moreover, several nonlinear kinematic hardening models have been proposed, as instance by Armstrong and Frederick (2007), introducing a nonlinear term to the linear rule allowing for a non-closed hysteresis loop (then resulting in a constant ratcheting rate). Chaboche et al. (1979, 1986) proposed then a "decomposed" nonlinear kinematic hardening rule superimposing several Armstrong and Frederick terms with the intention to describe a more realistic material behavior. Such model significantly improved the hysteresis loop description but still overpredicted the ratcheting behavior. Improvements to the original Chaboche model (1991) have been proposed but, however, the correct cyclic plasticity characterization is still a subject of ongoing research (Bari et al., 2000).

A nonlinear kinematic hardening model (Chaboche-type) has been adopted in this work for the characterization of the steel behavior, whereas a simpler linear kinematic hardening rule has been assumed for describing the behavior of CuCrZr alloy and braze.

2. Approach description

The proposed approach leverages on transient thermal-stress FEM analyses (ABAQUS FEM code was adopted in this work) of the most critical Baffle Modules (BMs, Fig. 4, Tab. 1), in order to extract the stress-strain results needed for the fatigue life estimate. The applied thermo-mechanical loads were those scheduled for the W7-X OP2: a pipe internal pressure (25 bar) of the coolant water and a uniform heat flux (250 kW/m²) radiated by the hot plasma on the graphite tiles.

Several critical positions were pointed out by preliminary FEM analyses and, for each of the ten most critical ones (the criticality was preliminary considered as the highest plastic strain), a FEM submodel was built up, in order to get the local stress-strain results with the highest possible accuracy, as needed to provide a reliable estimate of the related fatigue life.

Due to rigid interconnections among some BMs, the BM3h has been solved together with BM4h and BM5h (in order to take into account for the mutual interactions) whereas BM1v has been solved together with BM2v. The latter two modules exhibited a very low fatigue life in the interconnection when solved in the rigidly jointed configuration. Thus, it was necessary to redesign such interconnection and the previously adopted rigid connection was substituted by a flexible one, allowing for relative displacements between BMs 1v-2v without modifying the existing pipe framework. The results here presented are referring to those obtained solving BM1v and BM2v separately: the flexible interconnection was then approximated by FEM with a complete disconnection between the two modules.

Table 1: Critical locations submodelled by FEM.

Baffle Module BM	1h	5h	1v	2v	5v	7v	8v
Analysed location LR	4	1a	5	1, 2	4c	2d, 3d, 6c	3a

3. FEM input data

Baffle FEM models involve five different materials: stainless steel EN 1.4404 (SS316L), CuCrZr alloy, braze, sigraflex® and graphite. The thermomechanical properties (ITER, 2008; RCC-MR, 2007; Weil et al., 2008) for all the considered materials are listed in Tabs. 2-6, whereas, the elastic-plastic constitutive laws considered for copper alloy, steel and braze are shown in Figs. 5-7 respectively. Since the graphite tiles are loosely bolted onto the heat sinks, they do not contribute to the stress state of heat sinks and pipes and therefore were not modeled for the FEM stress analyses (no need of graphite and sigraflex® mechanical properties). In addition to the properties of Tabs. 2-6,

the orthotropic thermal conductivities of sigraflex® layers, modeled just as an interface condition between CuCrZr heat sinks and graphite tiles, are provided: (K_{11}, K_{22}, K_{33}) = (100, 3, 100) W/m/°C.

Table 2. CuCrZr thermomechanical properties.

T [°C]	20	100	200	300	400	600	700
E [GPa]	130	-	120	-	110	95	-
σYS [MPa]	297	286	268	246	222	161	125
α [1E-5/°C]	1.59	1.63	1.68	1.73	1.78	1.88	1.94
K [kW/m/°C]	0.379	-		0.351	-	-	0.372
cp [J/kg/°C]	388	-	-	-	-	-	473
ρ [kg/mm3]	8.92E-6	-	-	-	-	-	-
ν [-]	0.3	-	-	-	-	-	-

Table 3. Braze thermomechanical properties.

T [°C]	20	100	200	300	400	600	700
E [GPa]	214.3	-	-	-	183.3	-	158.3
σYS [MPa]	300	-	-	-	220	-	190
α [1E-5/°C]	1.59	1.63	1.68	1.73	1.78	1.88	1.94
K [kW/m/°C]	0.01	-	-	-	-	-	-
cp [J/kg/°C]	388	-	-	-	-	-	473
ρ [kg/mm3]	8.9E-6	-	-	-	-	-	-
ν [-]	0.3	-	-	-	-	-	-

Table 4. SS316L thermomechanical properties.

T [°C]	20	100	200	300	400	500	700
E [GPa]	158	152.7	146.15	139.04	-	133.51	-
σYS [MPa]	208.38	203.83	202.9	194.14	-	186.69	-
α [1E-5/°C]	1.59	1.63	1.68	1.73	1.78	1.88	1.94
K [kW/m/°C]	0.015	-	-	-	0.021	-	-
cp [J/kg/°C]	472	-	-	-	520	-	-
ρ [kg/mm3]	7.96E-6	-	-	-	-	-	-
ν [-]	0.3	-	-	-	-	-	-

Table 5. Graphite thermal properties.

T [°C]	20	100	300	500	700	1000	2200
K [kW/m/°C]	0.116	0.083	0.052	0.039	0.031	0.029	0.017
cp [J/kg/°C]	672	-	-	-	1830	1920	-
ρ [kg/mm3]	1.83E-6	-	-	-	-	-	-

Table 6. Sigraflex® thermal properties.

T [°C]	20	800	1000
cp [J/kg/°C]	740	1850	1950
ρ [kg/mm3]	1.1E-6	-	-

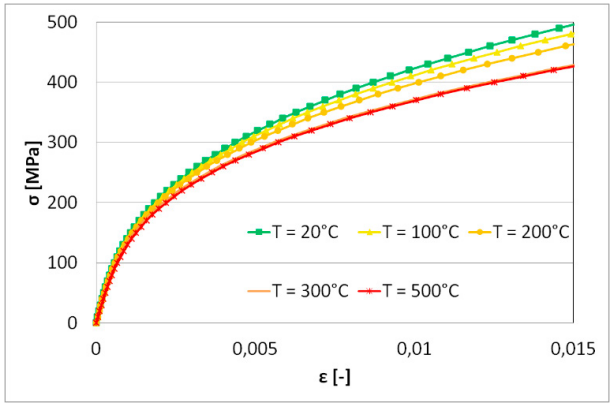

Fig. 5. Elastic-plastic true stress-strain curves for EN1.4404 (SS316L).

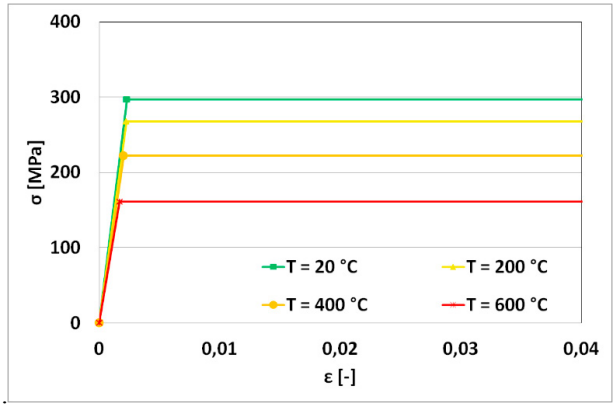

Fig. 6. Elastic-plastic true stress-strain curves for CuCrZr alloy.

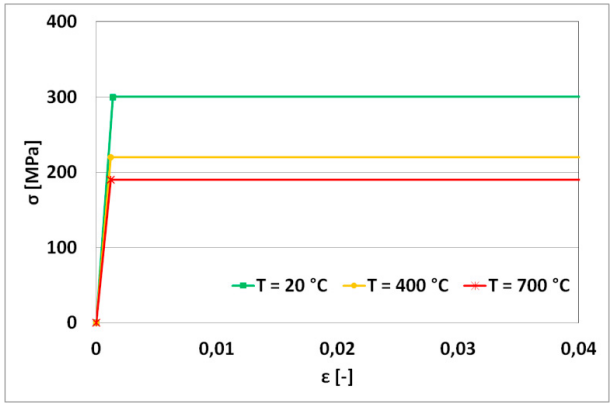

Fig. 7. Elastic-plastic true stress-strain curves for braze.

E is the Young's modulus, σ_{YS} is the yield stress, α is the thermal expansion coefficient, K is the thermal conductivity, c_p is the specific heat, ρ is the mass density and υ is the Poisson's ratio.

A nonlinear kinematic hardening model (Chaboche-type) in combination with the Mises yield surface was adopted to model the SS316L steel hardening. Such model is suitable for modelling inelastic deformations in most metals subjected to thermal and/or mechanical cycles, since its features allow accounting for Bauschinger effect,

cyclic hardening and mean stress relaxation. The model consists of a nonlinear kinematic hardening component that describes the translation of the Mises yield surface in the stress space through the backstress $\boldsymbol{\alpha}$. The stress is then computed as $\boldsymbol{E} * \boldsymbol{\varepsilon_{el}}$ until the yield surface is reached ($\boldsymbol{E}$ is the stiffness matrix and $\boldsymbol{\varepsilon_{el}}$ the elastic strain vector), whereas, the yield surface shift is governed by the backstress $\boldsymbol{\alpha} = \sum_i \boldsymbol{\alpha_i}$ where each $\boldsymbol{\alpha_i}$ is incrementally computed by means of the relation

$$\dot{\boldsymbol{\alpha_i}} = C_i \frac{1}{\sigma_0}(\boldsymbol{\sigma} - \boldsymbol{\alpha})\dot{\varepsilon_{pl}} - \gamma_i \boldsymbol{\alpha_i} \dot{\varepsilon_{pl}} , \quad (1)$$

where i is the number of backstresses $\boldsymbol{\alpha}_i$ (i = 3 as for the Chaboche model), $\boldsymbol{\sigma}$ is the deviatoric part of the stress tensor, C_i and γ_i are the hardening parameters (listed in Tab. 7) calibrated on the SS316L cyclic curves (Fig. 5) and $\dot{\varepsilon_{pl}}$ is the equivalent plastic strain rate computed as

$$\dot{\varepsilon_{pl}} = \sqrt{\frac{2}{3}\dot{\boldsymbol{\varepsilon_{pl}}} : \dot{\boldsymbol{\varepsilon_{pl}}}} . \quad (2)$$

For sake of simplicity, the cyclic behavior of CuCrZr and braze was modeled assuming pure linear kinematic hardening (Ziegler, 1959). In this model, a single backstress is computed as for Eq. 1 in which γ equal to 0 is considered; therefore, Eq. 1 changes for this case in

$$\dot{\boldsymbol{\alpha}} = C \frac{1}{\sigma_0}(\boldsymbol{\sigma} - \boldsymbol{\alpha})\dot{\varepsilon_{pl}} = \frac{\sigma_1 - \sigma_0}{\varepsilon_{pl,1}} \frac{1}{\sigma_0}(\boldsymbol{\sigma} - \boldsymbol{\alpha})\dot{\varepsilon_{pl}} , \quad (3)$$

where σ_1 and $\varepsilon_{pl,1}$ correspond to the σ and ε_{pl} values at ε = 0.04 of curves of Figs. 6, 7.

Further FEM input data were:

- coolant water temperature: 50 °C;
- braze conductance: 290 kW/m^{2}K;
- coolant water conductance: 15 kW/m^{2}K;
- contact conductance: 1 kW/m^{2}K.

Table 7. Temperature-dependent hardening parameters for SS316L.

T [°C]	20	100	200	300	500
C1 [MPa]	26200	5200	9600	40000	18500
γ1 [-]	562	1032	1	4750	1180
C2 [MPa]	10700	24100	17500	19000	18500
γ2 [-]	45	208	140	192	190
C3 [MPa]	11750	13100	18000	10300	10600
γ3 [-]	54	1	695	16	1

4. FEM analyses

The adopted FEM approach was based on sequentially coupled thermal-stress analyses for both global models and submodels (Fig. 8). For each of the ten considered locations, the adopted approach is based on a sequence of four nonlinear FEM analyses:

1. a global transient thermal analysis, to compute the BM temperature field;
2. a global steady-state thermal-stress analysis, to compute the BM stress-strain field using the temperature field from step 1;
3. a local transient thermal analysis, to compute the submodel temperature field using the thermal boundary conditions from step 1;
4. a local steady-state thermal-stress analysis, to compute the submodel stress-strain field using the mechanical boundary conditions from step 2 and the thermal boundary conditions from step 3.

The transient thermal analyses are used to compute the time-dependent temperature field on global and sub-models; it has been necessary to replicate the thermal analysis on the sub-model mesh since: (a) the braze root modelling has been added to the submodel geometry, (b) the global model meshes were too coarse for the subsequent analysis of step 4. Finally, the temperature fields of step 2 are applied as input thermal loads for the steady-state thermal-stress analyses in order to compute the time-dependent stress-strain fields (Fig. 8).

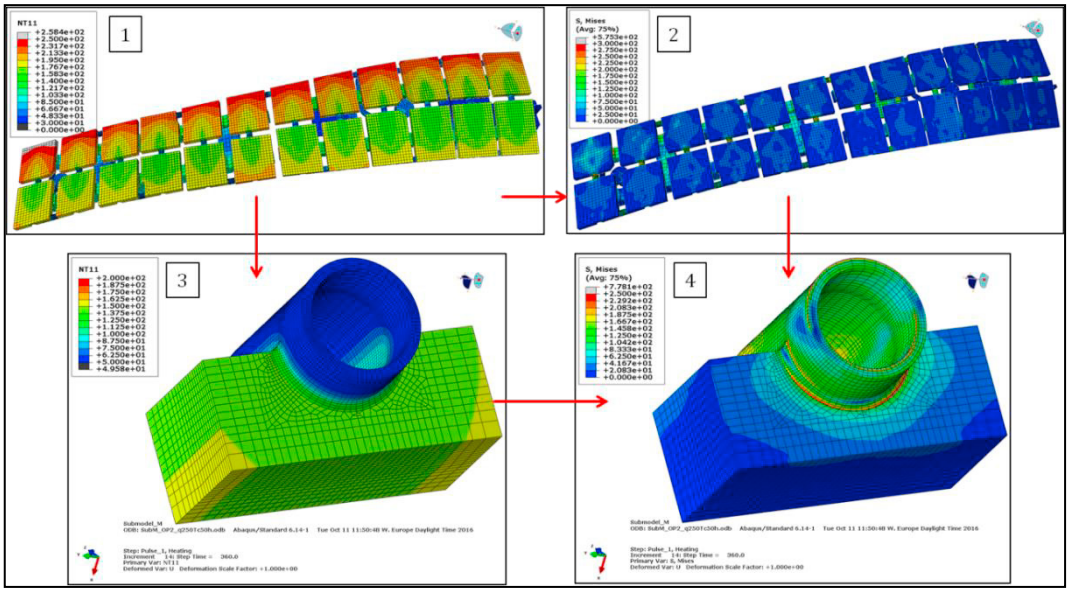

Fig. 8. Flowchart of the requested FEM analyses: (1) global thermal analysis, (2) global stress analysis, (3) local thermal analysis, (4) local stress analysis.

The heat flux, with magnitude equal to 250 kW/m^2, lasting an elapsed total time of 360 s, is uniformly radiated on the graphite tiles, which are explicitly modelled just for the thermal analyses. Such graphite tiles are loosely bolted on the CuCrZr heat sinks and therefore it is assumed that they do not contribute to the stress field. The baffles reach the steady-state conditions in less than 360 s, consequently, a 360 s loading application is also representative of a longer plasma pulse length. As a result, in order to evaluate the cyclic response of the modules, the FEM analyses consisted of sequences of heating/cooling cycles lasting 360 s each.

5. Multiaxial fatigue assessment

Fe-safe code was used to estimate the fatigue life of the most critical baffles of Fig. 4 in order to obtain a comparison with results related to the same problem and previously obtained using in house made routines.

Fe-safe code works as a postprocessor for the FEM results previously computed: the code reads the ABAQUS output files scanning for the stress-strain results either node-by-node or element-by-element. Afterwards, the fatigue life is estimated by means of the fatigue criterion selected in the fe-safe Graphical User Interface (GUI), reporting the results directly in ABAQUS log-life plots.

The ten considered submodels were separately imported into the fe-safe GUI and the previously obtained time-dependent stress-strain fields were imported as datasets for the subsequent fatigue assessments.

Two different fatigue criteria for multiaxial LCF problems were used in this work. All these criteria are so called “critical plane” criteria since the damage parameter, left term in Eq. 4, is repeatedly calculated (node-by-node) onto several planes with different orientations, thus leading to the definition of a “critical” plane on which the estimated fatigue life is the lowest. The adopted methods are:

Max shear strain: the damage parameter is the shear strain amplitude, $\Delta\gamma_{max}/2$, calculated onto the plane of maximum shear strain amplitude,

Brown-Miller: the damage parameter is a function of both shear and normal strains, $\Delta\varepsilon_n/2 + \Delta\gamma_{max}/2$, calculated onto the plane that experiences the maximum shear strain amplitude.

Moreover, a Morrow correction was adopted to take into account of the mean stress experienced by the material during the cycling; with the Morrow mean stress correction, the σ_f' of Eq. 4 becomes $(\sigma_f' - \sigma_m)$ to take into account such mean stress σ_m normal to the critical plane.

Mechanical and fatigue properties are shown in Figs. 5-7 and listed in Tabs. 2-7. The fatigue curve of Fig. 9 (RCC-MR, 2007) has been approximated with a Coffin-Manson type law (parameters in Tab. 8):

$$\left.\begin{matrix}\Delta\gamma_{max}/2 \\ \Delta\varepsilon_n/2 + \Delta\gamma_{max}/2\end{matrix}\right\} = C_1 \frac{\sigma_f'}{E}(2N_f)^b + C_2\varepsilon_f'(2N_f)^c \ , \tag{4}$$

where C_1 and C_2 are additional material parameters depending on the chosen criterion, here established as equal to 1.3 and 1.5 or 1.65 and 1.75 for Max shear strain and Brown-Miller criterion respectively.

Eq. 4 parameters have been inserted into fe-safe to obtain the fatigue life. N_f in Eq. 4 is the number of loading cycles ($2N_f$ is the number of load reversals), therefore, a full fatigue cycle of heating + cooling was defined in the analyses.

Table 8. SS316L fatigue parameters.

σ'f [MPa]	E [GPa]	ε'f [-]	b [-]	c [-]
560	158	0.08	-0.08	-0.53

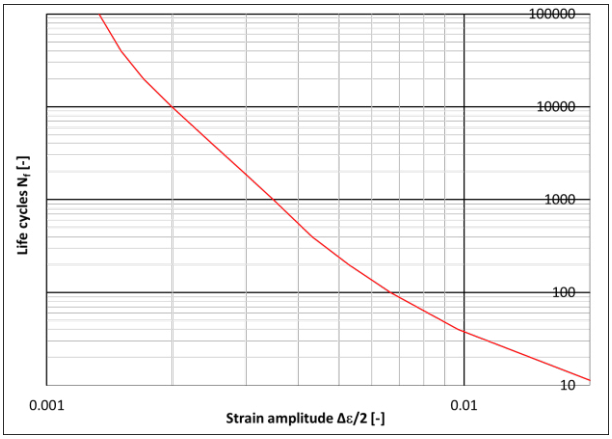

Fig. 9. Fatigue data for EN 1.4404 (SS316L) available from RCC-MR 2007 code.

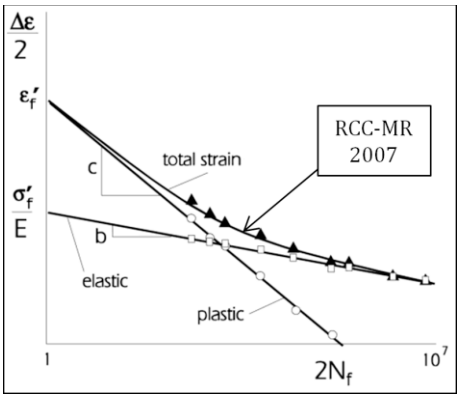

Fig. 10. Coffin-Manson type law.

6. Results

Fe-safe results are here reported in terms of fatigue life plots (no results were calculated for the heat sink or braze elements, Fig. 11). Plots are in logarithm to base 10, therefore a value of 3 stands for a life of 10^3 cycles. Finally, the fatigue lives are shown in Fig. 12 for all the adopted criteria and all the submodelled locations.

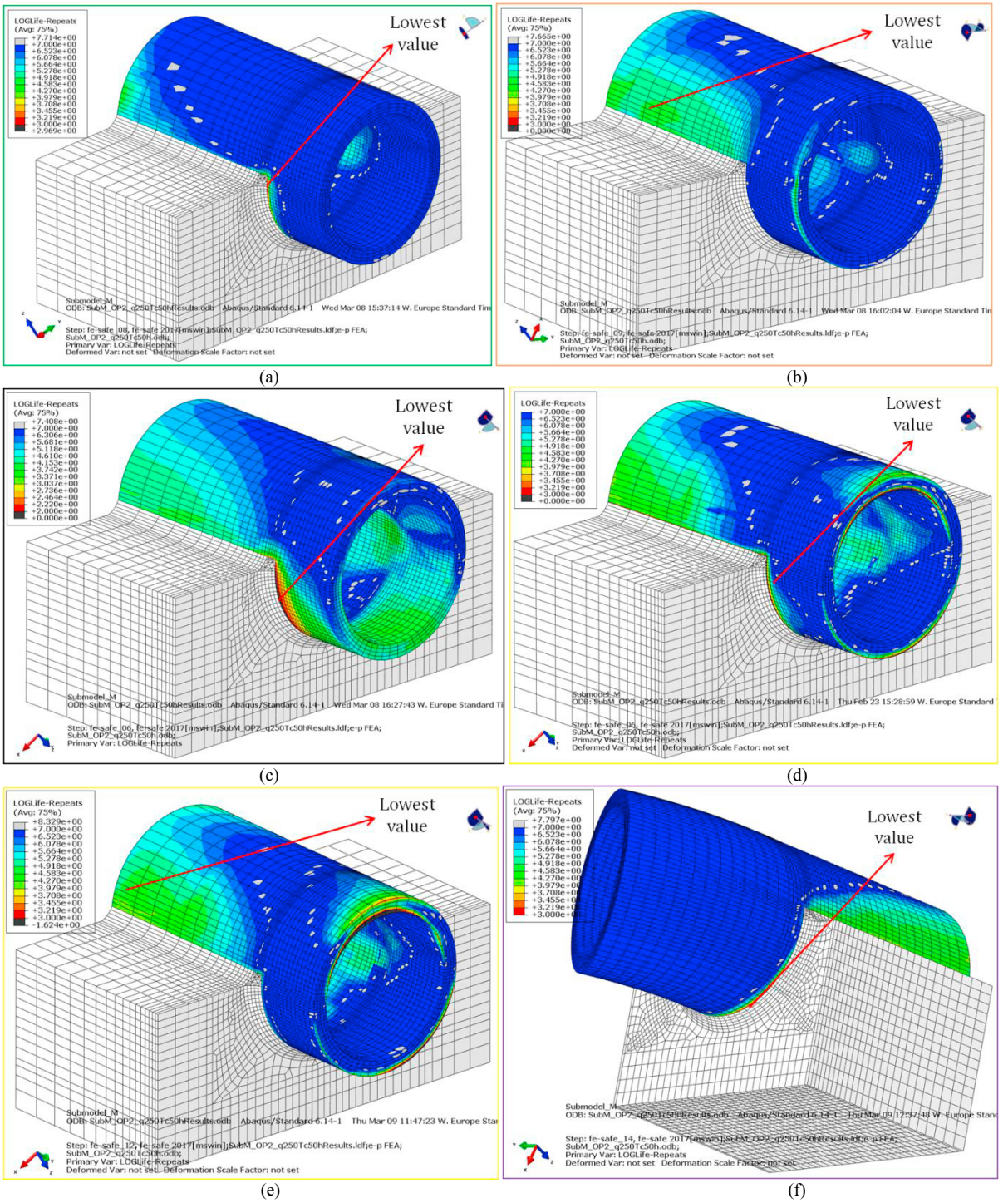

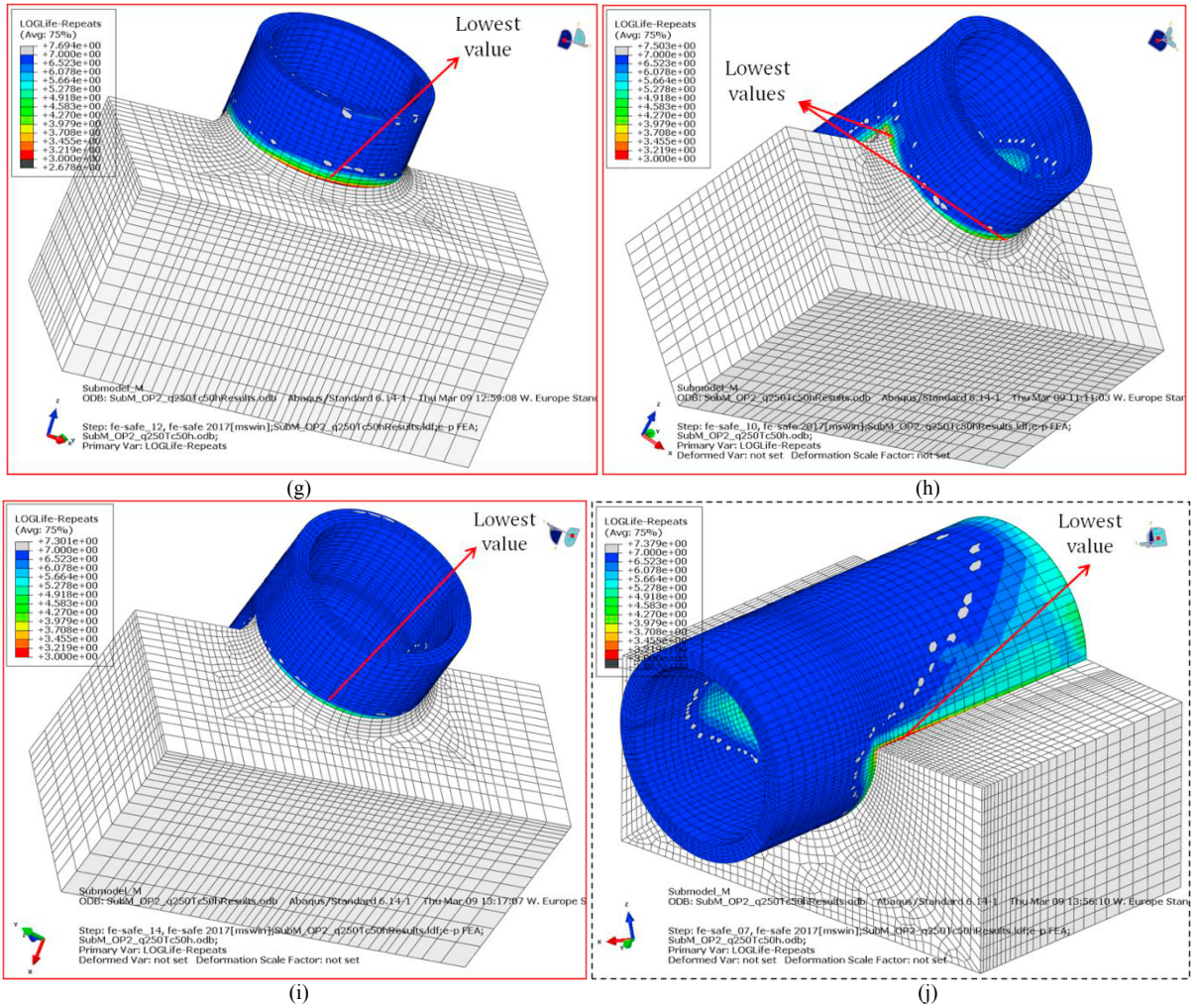

Fig. 11. Fe-safe fatigue life plots (adopting the Brown-Miller + Morrow criterion) for local models: (a) 1h-LR4, (b) 5h-LR1a, (c) 1v-LR5, (d) 2v-LR1, (e) 2v-LR2, (f) 5v-LR4c, (g) 7v-LR2d, (h) 7v-LR3d, (i) 7v-LR6c, (j) 8v-LR3a.

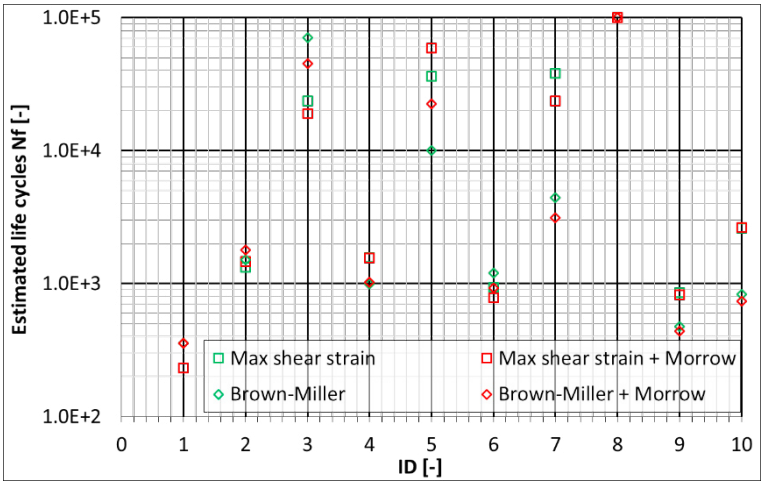

Fig. 12. Estimated fatigue lives for all the analysed locations; IDs from 0 to 9 are in turn: 1vLR5, 2vLR1, 2vLR2, 5vLR4c, 7vLR6c, 1hLR4, 7vLR3d, 5hLR1a, 7vLR2d, 8vLR3a.

7. Conclusions

A multiaxial Low-Cycle Fatigue approach has been used to estimate the fatigue life of the most critical baffle modules of W7-X when undergoing the OP2 loading conditions. Several critical locations were pointed out on the baffle modules by preliminary FEM analyses in which the damaging parameter was related to the plastic strain fluctuation. The most ten critical locations have been furtherly analysed by means of FEM submodels in order to get the highest accuracy on the results.

A uniform heat flux of 250 kW/m^2 has been applied on the graphite tiles to simulate by FEM the heat coming from the hot plasma. Such load has been considered in combination with the coolant water pressure and temperature. Material data come from come from ITER handbook and RCC-MR 2007 code.

A sequentially coupled thermal-stress FEM approach has been used to work out the transient thermal stress-strain fields on the entire baffle modules; then, a global-local FEM approach has been adopted to accurately evaluate the stress-strain fields in the critical areas. Finally, the fe-safe code has been used to estimate the fatigue live throughout all the submodels. Results in terms of estimated fatigue lives for all the analysed locations have been obtained with two different multiaxial fatigue criteria.

In case design heat loads of the baffles are confirmed in OP1.2, counter measures are required. One improvement could be to allow some flexibility between the rigid steel support and the heat sinks. Alternatively, a copper shield between the support structure and the baffles covering the steel pipes could reduce the thermal gradient in the cooling pipe so that the thermal deformation of the pipe matches that of the heat sink better.

References

Pedersen, T.S., et al., 2016. Confirmation of the topology of the Wendelstein 7-X magnetic field to better than 1:100,000. Nat. Commun. 7, 13493.

Klinger, T., et al., 2017. Performance and properties of the first plasmas of Wendelstein 7-X. Plasma Phys. Control. Fusion 59, 014018 (8pp).

Qian, X., et al., 2016. Assessment of the W7-X high heat flux divertor with thermo-mechanical analysis. Fusion Engineering and Design 109-111, 565-568.

Citarella, R., Giannella, V., Lepore, V., Dhondt, G., 2017. Dual boundary element method and finite element method for mixed-mode crack propagation simulations in a cracked hollow shaft. DOI: 10.1111/ffe.12655.

Citarella, R., Giannella, V., Lepore, M., 2015. DBEM crack propagation for nonlinear fracture problems. Frattura ed Integrità Strutturale 34, 514-523.

Giannella, V., Fellinger, J., Perrella, M., Citarella, R., 2017. Fatigue life assessment in lateral support element of a magnet for nuclear fusion experiment "Wendelstein 7-X". Engineering Fracture Mechanics 178, 243-257.

Citarella, R., Giannella, V., Lepore, M., Fellinger, J., 2016. FEM-DBEM procedure for crack analysis in baffle module of Wendelstein 7-X. WSEAS 11, E-ISSN: 2224-3429.

Citarella, R., Lepore, M., Fellinger, J., Bykov, V., Schauer, F., 2013. Coupled FEM-DBEM method to assess crack growth in magnet system of Wendelstein 7-X. Frattura ed Integrità Strutturale 26, 92-103.

Giannella, V., Perrella, M., Citarella, R., 2017. Efficient FEM-DBEM coupled approach for crack propagation simulations. DOI: 10.1016/j.tafmec.2017.04.003.

Citarella, R., Giannella, V., Vivo, E., Mazzeo, M., 2016. FEM-DBEM approach for crack propagation in a low pressure aeroengine turbine vane segment. Theoretical and Applied Fracture Mechanics 86 B, 143-152.

Prager, W., 1956. A new method of analyzing stresses and strains in work hardening plastic sol-ids. Journal of Applied Mechanics 23, 493-496.

Mroz, Z., 1967. On the description of anisotropic work hardening. Journal of the Mechanics and Physics of Solids 15, 163-175.

Armstrong, P.J., Frederick, C.O., 2007. A mathematical representation of the multiaxial bauschinger effect. Materials at High Temperatures 24(1), 1-26.

Chaboche, J.L., Dang-Van, K., Cordier, G., 1979. Modelization of the strain memory effect on the cyclic hardening of 316 stainless steel. Proceedings of the 5th International Conference on SMiRT, Div. L, Berlin, Germany.

Chaboche, J.L., 1986. Time-independent constitutive theories for cyclic plasticity. Int J Plast 2, 149-188.

Chaboche, J.L., 1991. On some modifications of kinematic hardening to improve the description of ratcheting effects. Int J Plast 7, 661-678.

Bari, S., Hassan, T., 2000. Anatomy of coupled constitutive models for ratcheting simulation. Int J Plast 16, 381–409.

Ziegler, H., 1959. A Modification of Prager's Hardening Rule. Quarterly of Applied Mathematics 17, 55-65.

ITER Material Properties Handbook, 2008, CuCrZr, ITER-AK02-CuCrZr.

RCC-MR, 2007, 1-Z-A3.4S.46.

Weil, K.S., Koeppel, B.J., 2008. Thermal stress analysis of the planar SOFC bonded compliant seal design. International Journal of Hydrogen Energy 33, 3976-3990.

RCC-MR, 2007, 1-Z-A3, 1-Z-A3.1S.